Unveiling the unique bifunctionality of $L1_2$-structured nanoprecipitates in a FeCoNiAlTi-type high-entropy alloy

Zhang, Jianyang; Zhao, Zhankun; Li, Qian; Luan, Junhua; Liu, Chain-Tsuan; Zhao, Yilu; Yang, Tao

Published in:
Advanced Powder Materials

Published: 01/07/2023

Document Version:
Final Published version, also known as Publisher's PDF, Publisher's Final version or Version of Record

Published version (DOI):
10.1016/j.apmate.2023.100113

Publication details:
Zhang, J., Zhao, Z., Li, Q., Luan, J., Liu, C.-T., Zhao, Y., & Yang, T. (2023). Unveiling the unique bifunctionality of $L1_2$-structured nanoprecipitates in a FeCoNiAlTi-type high-entropy alloy. *Advanced Powder Materials*, *2*(3), Article 100113. https://doi.org/10.1016/j.apmate.2023.100113

Advanced Powder Materials 2 (2023) 100113

Contents lists available at ScienceDirect

Advanced Powder Materials

journal homepage: www.keaipublishing.com/en/journals/advanced-powder-materials

Unveiling the unique bifunctionality of $L1_2$-structured nanoprecipitates in a FeCoNiAlTi-type high-entropy alloy

Jianyang Zhang [a], Zhankun Zhao [b], Qian Li [a,d], Junhua Luan [a], Chain-Tsuan Liu [a,c,d], Yilu Zhao [b,**], Tao Yang [a,d,e,*]

[a] Department of Materials Science and Engineering, Mechanical Behavior Division of Shenyang National Laboratory for Materials Science, City University of Hong Kong, Hong Kong, China
[b] School of Materials Science and Engineering, Harbin Institute of Technology, Shenzhen, China
[c] Department of Mechanical Engineering, City University of Hong Kong, Hong Kong, China
[d] Hong Kong Institute for Advanced Study, City University of Hong Kong, Hong Kong, China
[e] Hong Kong Branch of National Precious Metals Material Engineering Research Centre (NPMM), City University of Hong Kong, Hong Kong, China

ARTICLE INFO

Keywords:
High-entropy alloys
Precipitation strengthening
Mechanical properties
Deformation mechanisms
Martensitic transformation

ABSTRACT

Nanoprecipitation strengthening has been widely adopted as an effective way to design high-strength alloys, which generally leads to the loss of ductility. Here we unveil the unique bifunctionality of $L1_2$-structured nanoprecipitates in a FeCoNiAlTi-type high entropy alloy , enabling the combined increase of tensile strength and ductility. Results show that as-quenched precipitate-free matrix alloys undergo thermally-induced martensite transformation and form the body-centered cubic martensite phase with limited tensile ductility. In strong contrast, when introducing the dense coherent $L1_2$-type nanoprecipitates, the face-centered cubic matrix is temporarily stabilized, which in turn promotes the microbands-induced plasticity associated with stress-induced martensite transformation upon deformation. This allows us to achieve significantly improved work hardening capability and excellent plastic deformation stability at a high-strength level. These new findings reshape our understanding of the precipitation strengthening and could provide useful guidance for developing high-performance alloys by regulating the coherent nanoprecipitate and martensitic phase transformation.

1. Introduction

Precipitates are often used as strong dislocation obstacles for strengthening of materials. However, such obstacles generally lead to the decrease or even bankrupt of ductility, showing the so-called strength-ductility trade-off that has been a long-standing dilemma in materials science [1]. Excitingly, multicomponent $L1_2$-type nanoparticles in the high entropy alloys (HEAs) are recently found to exhibit intriguing bifunctional properties [2,3]. On one hand, it can provide coherent/ordered hardening to increase the strength of the materials in a similar way as the precipitates generally do. On the other hand, it appears that those multicomponent $L1_2$ precipitates are intrinsically ductile, which together with the ductile face-centered cubic (FCC) matrix enables a delicate modulation of ductilization mechanisms (such as microband-induced ductility, etc.) to be achieved in the precipitation-hardened HEAs [2]. Such unique features of the $L1_2$-strengthened HEAs offer a novel route toward superior strength-ductility synergy that could push the strength-ductility envelope into the previously inaccessible territory. One example is the FeCoNi-based HEAs with a high density of chemical complex $L1_2$ precipitates, which exhibit the high yield strength above 1 GPa with an excellent elongation over ~30% [2]. Those inspiring results have attracted significant interest in the development of advanced high-performance structural materials.

To date, numerous studies have focused on further improving the mechanical performance of precipitation-strengthened HEAs through micro-alloying [4,5] or novel thermo-mechanical processing [6–10]. The core strategies for strengthening lie in increasing the volume fraction of the precipitates as well as introducing back-stress hardening with respect to the heterogeneous microstructures. However, the ductilization

* Corresponding author. Department of Materials Science and Engineering, Mechanical Behavior Division of Shenyang National Laboratory for Materials Science, City University of Hong Kong, Hong Kong, China.
** Corresponding author.
E-mail addresses: zhaoyilu@hit.edu.cn (Y. Zhao), taoyang6-c@my.cityu.edu.hk (T. Yang).

https://doi.org/10.1016/j.apmate.2023.100113
Received 16 November 2022; Received in revised form 18 December 2022; Accepted 10 January 2023
Available online 11 February 2023

strategies (e.g. the twinning-induced plasticity, phase-transformation-induced plasticity, microband-induced plasticity, etc.) appear to be significantly distinctive from the single-phase alloys. For example, Zhao et al. [5] found that deformation-induced twinning was significantly suppressed by the presence of the $L1_2$ precipitates even though the overall stacking fault energy (SFE) of the HEA is low.

However, despite discoveries of mechanical twins or stacking faults during the deformation process, deformation-induced phase transformation is rarely found in the precipitation-strengthened HEAs. Indeed, precipitates are suggested to hinder phase transformation in many Fe-based alloys. Roca et al. [11] reported that $L1_2$ nano-precipitates in Fe–Mn–Al–Ni shape memory alloys can strongly shift the martensite-start temperature (M_s) to lower temperatures, leading to complete inhibition of thermally-induced martensite. Similarly, Yang et al. [12] found that rationally tuning the size and spacing of precipitates in Fe–Ni–Al–Ti alloys can partially hinder the formation of thermally-induced martensite, hence further inducing martensitic transformation during tensile testing, resulting in greatly enhanced work-hardening capability. More recently, we interestingly showcased that a small amount of FCC phase appeared to transform into BCC phase near the microband boundaries in a Fe–Co–Ni–Al–Ti HEA with a medium-to-high SFE, which could be indicative of a potential for modulating the deformation-induced phase transformation process in this HEA system [13]. Nevertheless, so far, the intrinsic phase transformation propensity of the matrix alloy remains unclear and how the $L1_2$ precipitates influence the phase transformation in the precipitation-strengthened HEAs is still far from being understood, which thereby requires more systematic analyses.

Therefore, in this study, we selected a precipitation-strengthened HEA with a nominal composition of $(FeCoNi)_{85.9}Al_8Ti_6B_{0.1}$ (at.%, denoted as Al8Ti6 HEA) as the model material. To evaluate the intrinsic phase transformation capability of the matrix alloy, an alloy with the matrix composition obtained from atom probe tomography (APT) analysis was also prepared by melting and thermo-mechanical processing (denoted as Al8Ti6 Matrix). The main objectives of this work are to unveil the effects of the $L1_2$ precipitates on the phase transformation, including the thermally-induced martensite and stress-induced martensite, as well as the deformation behaviors of alloys.

2. Results and discussion

Fig. 1(a) presents the electron backscatter diffraction (EBSD) image quality (IQ) superimposed the inverse pole figure (IPF) map of the Al8Ti6 HEA aged at 740 °C for 4 h, showing a fully recrystallized structure with an average grain size of ~50 μm. The inset in Fig. 1(a) is the

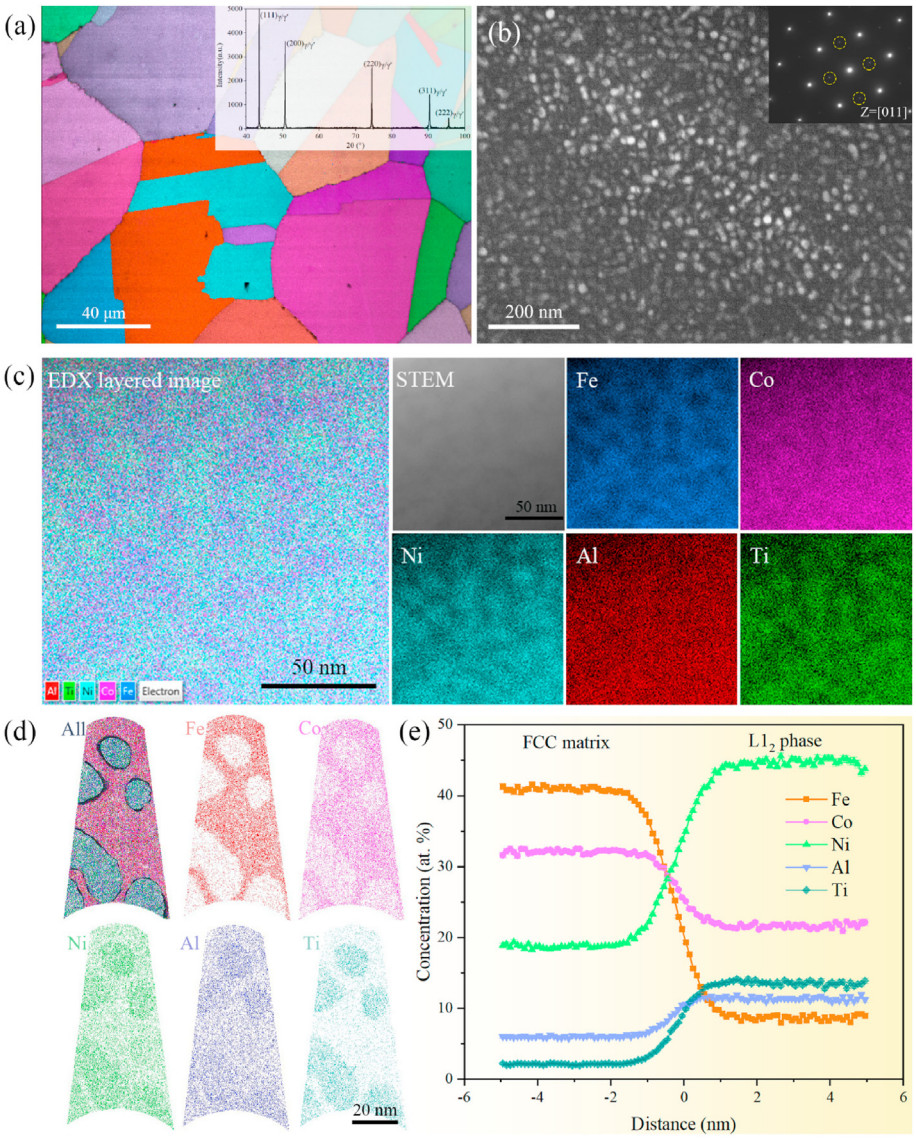

Fig. 1. Microstructure and chemical composition of the Al8Ti6 HEA. (a) EBSD image quality (IQ) overlaid with IPF map shows a fully recrystallized structure with an average grain size of ~50 μm. The dual-phase structure composed of FCC phase and $L1_2$ phase is shown by the XRD inset. (b) Dark-field TEM image of the $L1_2$ precipitates using the ordered superlattice spot (see inset, highlighted by yellow dashed circles). (c) STEM-EDX elemental mapping results for Fe, Co, Ni, Al, Ti, and the overlay of them. (d) A set of atom maps showing the elemental distribution between the $L1_2$ precipitates and FCC matrix. The $L1_2$/FCC interfaces are highlighted using a 8 at.% Ti iso-composition surface. (e) Proximity histogram delineating compositional profile across the precipitates/matrix interface.

corresponding X-Ray Diffraction (XRD) pattern, only the dual-phase structure of FCC + $L1_2$ was identified, and no BCC martensite was detected. A representative dark-field transmission electron microscope (TEM) image is shown in Fig. 1(b), using the superlattice spots of $L1_2$ precipitates, demonstrated in the selected area electron diffraction (SAED) pattern (see inset in Fig. 1(b)). Obviously, high-density nano-sized spherical $L1_2$ particles are uniformly distributed in the FCC matrix. The average radius of the nanoparticles is statistically measured to be 15.45 ± 3.44 nm. Both scanning TEM-energy dispersive X-ray (STEM-EDX) mapping and APT were used to characterize the elemental differences between the $L1_2$ precipitates and the FCC matrix. As shown in Fig. 1(c), Ni, Al, and Ti are preferentially partitioned into the $L1_2$ precipitates, while Fe and Co are more likely to partition into the FCC matrix. A more quantitative compositional analysis at the near-atomic scale of the alloy was further characterized by APT. Fig. 1(d) shows a set of atom maps containing all elements and the corresponding individual element, highlighted by iso-composition surfaces delineating regions containing more than 8 at.% Ti. Fine scale Ni–Al–Ti-riched particles can be clearly observed. The corresponding proximity histogram revealing the compositional profile across the $L1_2$ precipitates/FCC matrix interface was provided in Fig. 1(e), and the detailed results were summarized in Table 1. Consistent with our STEM-EDX observations, the APT elemental analysis confirms again that the $L1_2$ precipitates are enriched in Ni, Al, and Ti (Composition: $Ni_{45.1}Co_{21.8}Fe_{8.6}Al_{11.3}Ti_{13.2}$, at.%), while the FCC matrix holds a Fe and Co enriched composition of $Fe_{40.9}Co_{31.9}Ni_{19.0}Al_{6.2}Ti_{2.0}$ (at.%). The volume fraction and number density of $L1_2$ precipitates were calculated as 37% and 2×10^{23} m^{-3}, respectively.

Fig. 2(a) displays the EBSD IQ map overlaid with IPF map of the Al8Ti6 Matrix. Interestingly, distinctive from the FCC structure revealed in the case of Al8Ti6 HEA with nano-precipitates (see Fig. 1), the detached Al8Ti6 Matrix exhibits a full martensitic structure (up to 50 μm in length) with no retained austenite phase when thermally quenched to room temperature. The formation of the thermally-induced BCC martensite lath was also confirmed by the inset XRD pattern in Fig. 2(a), where all the diffraction peaks are exclusively assigned to the BCC structure. A typical bright-field TEM image and the corresponding SAED pattern (using the $[\bar{1}11]$ zone axis) were shown in Fig. 2(b), indicating that the lath martensite in as-quenched Al8Ti6 Matrix is composed of a high density of dislocations. Such lath martensitic microstructures have also been observed in some metastable Fe–C alloys [14–16] and maraging steels [17–19]. Additionally, the elemental distribution between lath martensite was given in Fig. 2(c). It can be seen from this STEM EDX mapping that each element is evenly distributed in the distinctly oriented lath martensite. This observation is supported by the line profile of compositional variation along the yellow arrow in Fig. 2(c), as shown in Fig. 2(d). This homogenous distribution of elements between lath martensite confirms the diffusionless martensitic transformation from high-temperature FCC phase (paramagnetic state) to BCC phase (ferromagnetic state) [12,20]. For the present Al8Ti6 Matrix, it has been well established that most alloying elements other than Co, Al, and Ti lower the martensite-start temperature. The effect of chemical composition on the M_s temperature of Fe-based alloys was expressed by Ref. [21].

Table 1
Chemical compositions of the precipitates and the matrix in the Al8Ti6 HEA.

Alloy	Phases	Compositions (at.%)					
		Fe	Co	Ni	Al	Ti	B
Al8Ti6	Nominal	28.63	28.63	28.63	8	6	0.1
	Matrix	40.91 ± 0.27	31.93 ± 0.26	19.03 ± 0.21	6.17 ± 0.13	1.96 ± 0.07	–
	$L1_2$	8.62 ± 0.23	21.78 ± 0.35	45.11 ± 0.43	11.29 ± 0.26	13.19 ± 0.29	–

$$M_s(^\circ C, at.\%) = 545 - 71C + Al + 7Co - 14Cr - 15Cu - 23Mn - 8Mo - 6Nb - 13Ni - 4Si + 3Ti - 4V + 0W$$

Because of its much higher Co content and relatively lower Ni content, the M_s temperature of Al8Ti6 Matrix can be estimated to be around 500 °C (well above the room temperature), which accounts for the complete martensitic phase transformation occurred in the Al8Ti6 Matrix at room temperature. Evidently, compared to the scenario of the Al8Ti6 HEA with dense $L1_2$ nanoparticles, it can be concluded that the presence of these nanoparticles can greatly suppress the otherwise favored martensitic transformation and thus temporarily stabilize the FCC matrix in the Al8Ti6 HEA during water-quenching. Such a behavior was similar to that in some Fe-based shape memory alloys containing precipitates [11].

Room temperature tensile stress-strain curves for the Al8Ti6 HEA and Al8Ti6 Matrix are given in Fig. 3. The yield strength and uniform elongation of Al8Ti6 HEA are 974 ± 15 MPa and ~40%, respectively, while the yield strength of Al8Ti6 Matrix is 986 ± 21 MPa, with almost no uniform elongation. Obviously, compared to the severe plastic instability exhibited by the Al8Ti6 Matrix, the $L1_2$-strengthened Al8Ti6 HEA exhibits a good combination of strength and ductility, high strain hardening, and excellent uniform deformation without premature fracture. Furthermore, the insets show the low-magnification fracture surfaces, respectively, wherein the Al8Ti6 Matrix exhibits obvious local necking behavior, while no serious macroscopic necking occurs in the Al8Ti6 HEA. The corresponding high-magnification fracture surfaces are given in Fig. 3(b) and **(c)**, a relatively flat surface consisting of numerous small dimples and a rugged surface with many large dimples are observed in Al8Ti6 HEA and Al8Ti6 Matrix, respectively.

To discern the underlying micro-mechanisms for the excellent mechanical properties and high work-hardening capacity of Al8Ti6 HEA, we further analyzed the deformation behaviors of the specimens after fracture using the high-resolution EBSD and TEM. From left to right, Fig. 4(a) shows the EBSD IQ, IPF, kernel average misorientation (KAM), and phase maps of the Al8Ti6 HEA after fracture. The IPF map reveals a subtle misorientation change within <101> grain interior during the tensile straining. This can be more intuitively observed by the KAM map, where localized strain occurs in some regions. From the phase map, it seems that no deformation-induced phase transformation occurs after fracture, and the phase structure of FCC + $L1_2$ is still well maintained. The misorientation profile calculated along the white dashed arrow of the IQ map in Fig. 4(a) was provided in Fig. 4(b). The low-angle grain boundaries due to local misorientation changes caused by severe straining can be clearly evidenced, which are in good agreement with the IPF and KAM observations. Furthermore, a typical bright-field TEM image, as shown in Fig. 4(c), demonstrates that nano-spaced deformation-induced microbands emerge as the prevalent deformation mode in Al8Ti6 HEA at the late stage of deformation. The inset SAED pattern in Fig. 4(c) along the [011] zone axis confirms the absence of deformation twinning and further confirms the presence of microbands as low-angle grain boundaries (see the elongated spots due to deviation from exact Bragg diffraction). This deformation behavior of microbands accommodating plastic deformation at elevated loads is consistent with our previous results [2,13], and is also observed as the dominant deformation mode in many high manganese steels [22–24]. It has been suggested that the well-developed deformation-induced microbands can not only redistribute and enhance the storage of dislocations at the parallel slip planes but also offer a pathway for stress delocalization by pronounced cross-slip events, resulting in a continuous and stable plastic deformation [25]. On the other hand, the presence of the nano-spaced microbands contributes to strengthening by reducing the mean free path of dislocations (the so-called dynamic Hall-Petch effect), which helps to postpone the onset of necking instability without premature fracture. However, the Al8Ti6 Matrix with the martensitic structure exhibits almost no work hardening capability due to the fewer independent activated slip systems,

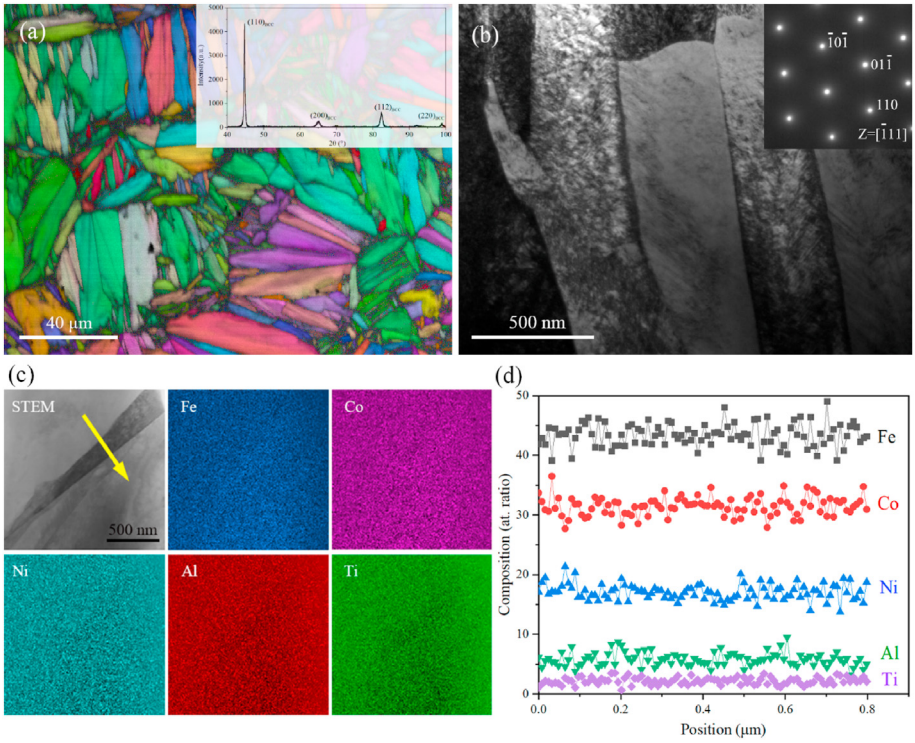

Fig. 2. Microstructure analysis of the Al8Ti6 Matrix. (a) The EBSD IQ plus IPF showing the thermally-induced martensite in the as-quenched state. The inset XRD pattern showing the BCC phase structure with lattice constant a = 0.286 nm. (b) Bright-field TEM image of the lath martensite, the inset shows the SAED pattern using [$\bar{1}$11] zone axis. (c) STEM–EDX mapping showing the uniform distribution of different elements among lath martensites. (d) STEM–EDX line scan along the yellow arrow in (c) further demonstrates the diffusionless phase transformation from FCC structure to BCC structure.

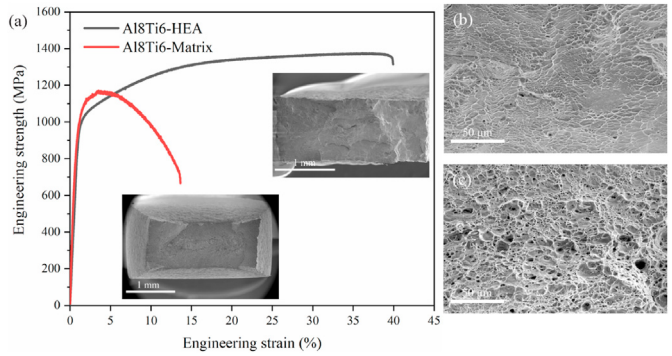

Fig. 3. (a) Room-temperature tensile stress-strain curves for Al8Ti6 HEA and Al8Ti6 Matrix. The insets show the low-magnification fracture surfaces, respectively, wherein Al8Ti6 Matrix exhibits severe necking, while no visible necking occurs in the Al8Ti6 HEA. High-magnification fracture surfaces reveal ductile dimples of the Al8Ti6 HEA (b) and Al8Ti6 Matrix (c), respectively.

leading to rapid strain localization and the early onset of plastic instability (see the inset in Fig. 3(a)).

A more in-depth and careful analysis of the deformation behavior was performed by high-resolution TEM. We found that the nano-sized deformation-induced martensite appears in the vicinity of certain microbands, as shown in Fig. 5(a). In addition to the $L1_2$ (in purple) and FCC regions (in red), the projected atomic column along the [011] zone axis clearly shows the appearance of deformation-induced BCC martensite regions (in cyan) around the microbands. These regions are further confirmed by the associated fast Fourier transform (FFT) patterns, and it can be obtained that both the FCC/BCC interface and the $L1_2$/BCC interface exhibit a Nishiyama-Wasserman orientation, namely, $\{111\}_{FCC/L12}||\{011\}_{BCC}$ and $<011>_{FCC/L12}||<001>_{BCC}$ [26]. Since the scale of deformation-induced BCC martensite is only a few nanometers wide, it is thus difficult to detect them even by using the high-resolution EBSD (see the phase map in Fig. 4(a)).

The excellent work-hardening capability brought about by deformation-induced martensite has been widely studied in medium or low manganese steels [27] and titanium alloys [28], but is rarely observed in precipitation-strengthened HEAs. In the present Al8Ti6 HEA with a medium-to-high SFE (53 mJ/m^2) [13], the dense $L1_2$ particles seem to completely hinder the generation of thermally-induced BCC martensite during quenching, and also greatly suppress the deformation-induced martensite during tensile testing. However, since the microbands dominated the deformation due to the frequent screw dislocations cross-slip caused by the medium-to-high SFE [2,13], deformation-induced martensite appeared near the highly distorted and localized strain fields generated by microbands (see Fig. 5 (b)). The deformation-induced martensite as an additional carrier for plasticity further promotes the sustained and stable deformation of the Al8Ti6 HEA under high straining. Similar experimental results were observed by Li et al. [29] in their study of the low-cycle fatigue properties of nano-twinned 316L stainless steel, the fatigue-induced martensite was formed in micro-shear bands after fatigue fracture at high strain amplitude, which effectively relieved the stress concentration.

Based on the above analysis, our experimental observations regarding the effect of bifunctional $L1_2$-structured particles on the alloys are summarized and illustrated schematically in Fig. 6. It can be seen that the austenite phase without nanoprecipitates (the Al8Ti6 Matrix) at elevated temperature directly transforms into the thermally-induced BCC martensite after quenching to room temperature, and remains martensitic structure after fracture. However, the austenite phase decorated by $L1_2$ nano-precipitates (Al8Ti6 HEA) at this temperature can be well maintained as the austenite-plus-precipitate microstructure after quenching to room temperature, which can be ascribed to the hindering effect of dense $L1_2$ precipitates on the thermally-induced martensite phase transformation. Under high-stress loading conditions, although $L1_2$ precipitates still suppress most of the stress-induced martensite, the numerous microbands and accompanying stress-induced martensite become the additional deformation mode in the Al8Ti6 HEA.

3. Conclusion

In summary, through the multiscale characterization techniques, we

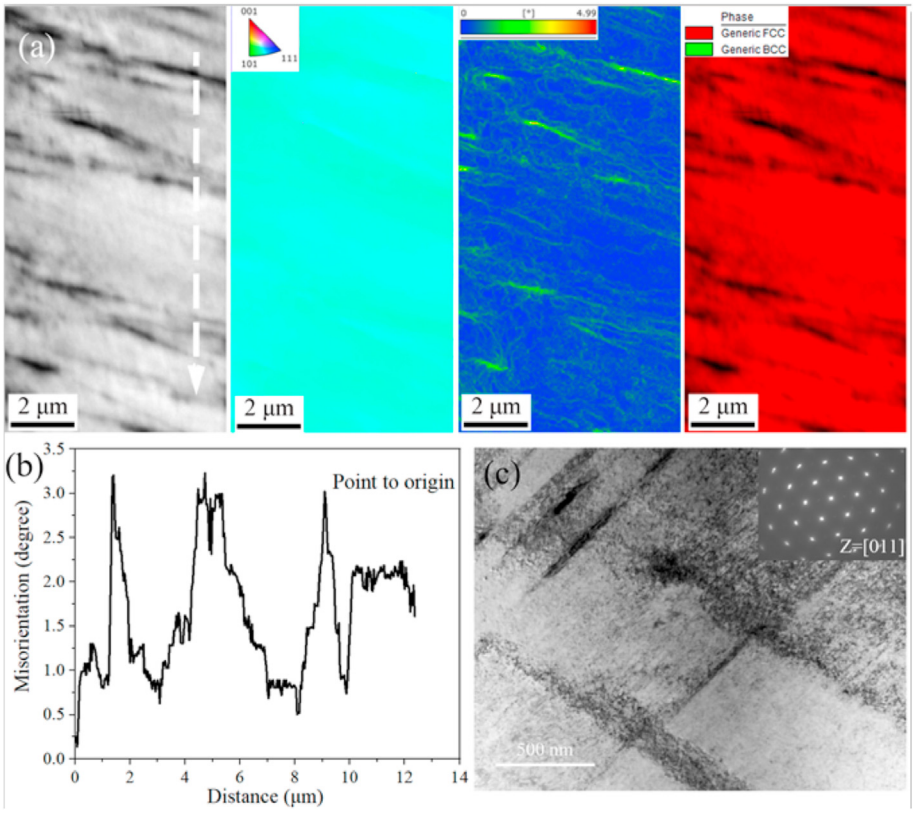

Fig. 4. (a) From left to right, EBSD IQ, IPF, kernel average misorientation (KAM), and phase map of Al8Ti6 HEA after tensile to fracture. (b) Corresponding plot of the misorientation variation along the white arrow in (a), measured with respect to from point to origin. (c) A typical bright-field TEM micrograph shows deformation-induced microbands formed in Al8Ti6 HEA after fracture, and the inset shows the SAED pattern of the microbands along the [011] zone axis, which indicates crystal rotation near the microbands.

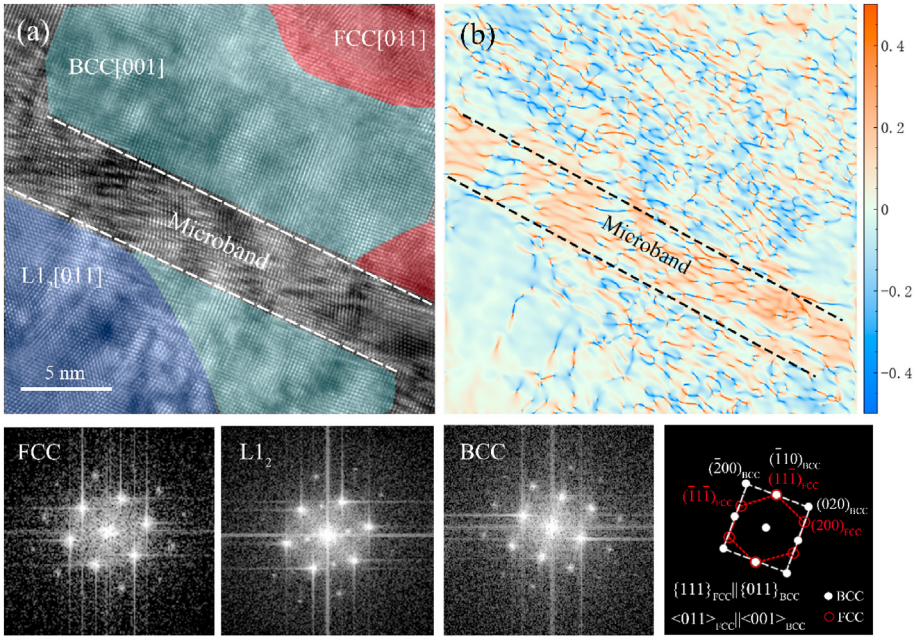

Fig. 5. (a) High-resolution TEM image and the associated fast Fourier transform (FFT) pattern showing the deformation-induced BCC martensite (cyan), $L1_2$ (purple), and FCC (red) regions near the microband in Al8Ti6 HEA after fracture, projected along the [011] beam direction. Both the FCC/BCC interface and the $L1_2$/BCC interface exhibit a Nishiyama-Wasserman orientation, namely, $\{111\}_{FCC/L12}||\{011\}_{BCC}$ and $<011>_{FCC/L12}||<001>_{BCC}$. (b) Corresponding geometric phase analysis (GPA) strain map (in-plane rigid-body rotation, w_{xy}) for HRTEM image (a).

demonstrated that the dense $L1_2$ precipitates in Al8Ti6 HEA can not only provide conventional precipitation strengthening, but also suppress the appearance of thermally-induced martensite during water quenching and temporarily stabilize the FCC structure of the matrix. Moreover, the medium-to-high SFE of Al8Ti6 HEA makes it possible for frequent dislocation cross-slip in the late stage of deformation, resulting in microbands-dominated deformation mode at higher plastic strains. The nano-sized stress-induced martensite appears near the microbands, which in turn can facilitate the stress relief and further enhance the sustainable work-hardening capability and uniform deformation, delaying the onset of necking instability. Our findings not only deepen the fundamental understanding of bifunctionality of the nanoprecipitation in HEAs, but also would provide new insight into the development of novel alloys with outstanding mechanical properties based on the nanoprecipitation-tailored phase transformation.

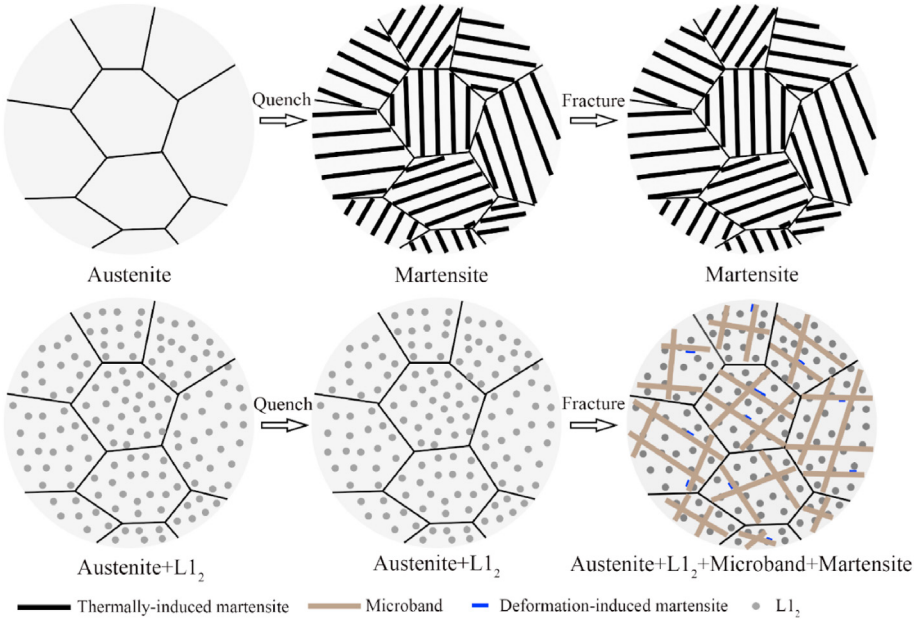

Fig. 6. The schematic illustration showing the austenite phase without precipitates (Al8Ti6 Matrix) at high temperature transforms into the thermally-induced martensite after quenching to room temperature, and remains martensite after fracture. The austenite phase decorated by $L1_2$ nano-precipitates (Al8Ti6 HEA) at high temperature still maintains the austenite-plus-precipitate microstructure after quenching to room temperature, the multiple microbands and accompanying deformation-induced martensite appear after fracture.

4. Experimental details

The alloys with nominal composition of $(FeCoNi)_{85.9}Al_8Ti_6B_{0.1}$ (at.%) were prepared via arc melting high purity (>99.9 wt%) raw materials. The arc-melted buttons were flipped and re-melted at least five times to ensure the chemical homogeneity, followed by drop-casting into a copper mould to produce rectangular ingots with a dimension of 5 × 12 × 60 mm^3. The as-cast ingots were homogenized at 1150 °C for 2 h before cold rolling into 1.7-mm-thick plates at room temperature. Equiaxed grain microstructures with an average grain size of about 50 μm were obtained by recrystallization at 1150 °C for 1.5 min. After aging at 740 °C for 4 h, the composition of the matrix of Al8Ti6 HEA was quantitatively determined by APT, i.e., $Fe_{40.9}Co_{31.9}Ni_{19.0}Al_{6.2}Ti_{2.0}$ (at.%, denoted as Al8Ti6 Matrix). The Al8Ti6 Matrix alloy (with the same composition as the matrix of the Al8Ti6 HEA) was then produced and processed identically to the Al8Ti6 HEA. All the heat treatment procedures described here were finished by water quenching.

Subsequently, the dog-bone-shaped specimens with a gauge length of 12.5 mm and a cross-sectional dimension of 3.2 × 1.5 mm^2 were prepared by electric discharge cutting. Uniaxial tensile tests were performed on a Material Testing System (MTS, Alliance RT30) machine with an engineering strain rate of 1×10^{-3} s^{-1} at ambient temperature. The X-Ray Diffraction (XRD) was carried out on a Bruker D2-Phaser instrument. Microstructure characterization was conducted using scanning electron microscopy (SEM, Quanta FEG450) in conjunction with high-resolution electron backscatter diffraction (EBSD) and transmission electron microscope (TEM, JEOL 2100F). The specimens prepared for TEM observation followed the standard process of grinding, ion thinning, and final polishing. The strain distribution of the deformed specimen was mapped based on geometric phase analysis (GPA) of its high-resolution TEM (HRTEM) image, performed by the open-source program Strain ++ [30]. The elemental analysis was investigated using both the scanning TEM-energy dispersive X-ray (STEM-EDX) and APT. Sharp-tip specimens for APT test were prepared using a FEI Scios focused ion beam/scanning electron microscope (FIB/SEM). APT probing was performed on a local electrode atom probe (CAMECA LEAP 5000XR) under the ultra-high vacuum condition with a 20% pulse fraction and a 200 kHz pulse rate, at a cryogenic temperature of 70 K. Data reconstruction was performed using the commercial software package IVAS 3.8.4.

Data availability

The raw/processed data required to reproduce these findings cannot be shared at this time as the data also forms part of an ongoing study.

Acknowledgements

The authors from the City University of Hong Kong greatly acknowledge the financial supports from the National Natural Science Foundation of China (No. 52101151), the Hong Kong Research Grant Council (RGC) (Grant No. CityU 21205621 and C1020-21G), and the Shenzhen Science and Technology Program (Grant No. SGDX20210823104002016). Y.L. Zhao from the Harbin Institute of Technology (Shenzhen) thanks to the financial support from the National Natural Science Foundation of China (No. 52101135) and the Shenzhen Science and Technology Program (Grant No. RCBS20210609103202012).

References

[1] R.O. Ritchie, The conflicts between strength and toughness, Nat. Mater. 10 (2011) 817–822.
[2] T. Yang, Y.L. Zhao, Y. Tong, Z.B. Jiao, J. Wei, J.X. Cai, X.D. Han, D. Chen, A. Hu, J.J. Kai, K. Lu, Y. Liu, C.T. Liu, Multicomponent intermetallic nanoparticles and superb mechanical behaviors of complex alloys, Science 362 (2018) 933–937.
[3] T. Yang, Y.L. Zhao, W.P. Li, C.Y. Yu, J.H. Luan, D.Y. Lin, L. Fan, Z.B. Jiao, W.H. Liu, X.J. Liu, J.J. Kai, C.T. Liu, Ultrahigh-strength and ductile superlattice alloys with nanoscale disordered interfaces, Science 369 (2020) 427–432.
[4] J.Y. He, H. Wang, H.L. Huang, X.D. Xu, M.W. Chen, Y. Wu, X.J. Liu, T.G. Nieh, K. An, Z.P. Lu, A precipitation-hardened high-entropy alloy with outstanding tensile properties, Acta Mater. 102 (2016) 187–196.
[5] Y.L. Zhao, T. Yang, Y. Tong, J. Wang, J.H. Luan, Z.B. Jiao, D. Chen, Y. Yang, A. Hu, C.T. Liu, J.J. Kai, Heterogeneous precipitation behavior and stacking-fault-mediated deformation in a CoCrNi-based medium-entropy alloy, Acta Mater. 138 (2017) 72–82.
[6] B. Gwalani, S. Dasari, A. Sharma, V. Soni, S. Shukla, A. Jagetia, P. Agrawal, R.S. Mishra, R. Banerjee, High density of strong yet deformable intermetallic nanorods leads to an excellent room temperature strength-ductility combination in a high entropy alloy, Acta Mater. 219 (2021), 117234.
[7] C. Zhang, C. Zhu, P. Cao, X. Wang, F. Ye, K. Kaufmann, L. Casalena, B.E. MacDonald, X. Pan, K. Vecchio, E.J. Lavernia, Aged metastable high-entropy alloys with heterogeneous lamella structure for superior strength-ductility synergy, Acta Mater. 199 (2020) 602–612.
[8] Y.J. Liang, L. Wang, Y. Wen, B. Cheng, Q. Wu, T. Cao, Q. Xiao, Y. Xue, G. Sha, Y. Wang, Y. Ren, High-content ductile coherent nanoprecipitates achieve ultrastrong high-entropy alloys, Nat. Commun. 9 (2018) 1–8.

[9] L. Fan, T. Yang, Y. Zhao, J. Luan, G. Zhou, H. Wang, Z. Jiao, C.T. Liu, Ultrahigh strength and ductility in newly developed materials with coherent nanolamellar architectures, Nat. Commun. 11 (2020) 1–8.
[10] B.X. Cao, H.J. Kong, L. Fan, J.H. Luan, Z.B. Jiao, J.J. Kai, T. Yang, C.T. Liu, Heterogenous columnar-grained high-entropy alloys produce exceptional resistance to intermediate-temperature intergranular embrittlement, Scripta Mater. 194 (2021), 113622.
[11] P. La Roca, A. Baruj, C.E. Sobrero, J.A. Malarria, M. Sade, Nanoprecipitation effects on phase stability of Fe–Mn–Al–Ni alloys, J. Alloys Compd. 708 (2017) 422–427.
[12] Y. Yang, T.Y. Chen, L.Z. Tan, J.D. Poplawsky, K. An, Y.L. Wang, G.D. Samolyuk, K. Littrell, A.R. Lupini, A. Borisevich, E.P. George, Bifunctional nanoprecipitates strengthen and ductilize a medium-entropy alloy, Nature 595 (2021) 245–249.
[13] Y.L. Zhao, Y.R. Li, G.M. Yeli, J.H. Luan, S.F. Liu, W.T. Lin, D. Chen, X.J. Liu, J.J. Kai, C.T. Liu, T. Yang, Anomalous precipitate-size-dependent ductility in multicomponent high-entropy alloys with dense nanoscale precipitates, Acta Mater. 223 (2022), 117480.
[14] S. Djaziri, Y. Li, G.A. Nematollahi, B. Grabowski, S. Goto, C. Kirchlechner, A. Kostka, S. Doyle, J. Neugebauer, D. Raabe, G. Dehm, Deformation-induced martensite: a new paradigm for exceptional steels, Adv. Mater. 28 (2016) 7753–7757.
[15] Y. Lu, H. Yu, R.D. Sisson Jr., The effect of carbon content on the c/a ratio of as-quenched martensite in Fe–C alloys, Mater. Sci. Eng. A 700 (2017) 592–597.
[16] T. Tanaka, N. Maruyama, N. Nakamura, A.J. Wilkinson, Tetragonality of Fe–C martensite—a pattern matching electron backscatter diffraction analysis compared to X-ray diffraction, Acta Mater. 195 (2020) 728–738.
[17] S.H. Jiang, H. Wang, Y. Wu, X.J. Liu, H.H. Chen, M.J. Yao, B. Gault, D. Ponge, D. Raabe, A. Hirata, M.W. Chen, Y.D. Wang, Z.P. Lu, Ultrastrong steel via minimal lattice misfit and high-density nanoprecipitation, Nature 544 (2017) 460–464.
[18] H. Li, Y. Liu, B. Liu, D.X. Wei, Synergistic enhancement of strength and ductility of cobalt-free maraging steel via nanometer-scaled microstructures, Mater. Sci. Eng. A 842 (2022), 143099.
[19] D. Raabe, D. Ponge, O. Dmitrieva, B. Sander, Nanoprecipitate-hardened 1.5 GPa steels with unexpected high ductility, Scripta Mater. 60 (2009) 1141–1144.
[20] Y.L. Chen, W.L. Xiao, K. Jiao, D.H. Ping, H.B. Xu, X.Q. Zhao, Y.Z. Wang, Cubic martensite in high carbon steel, Phys. Rev. Mater. 5 (2018), 050601.
[21] K. Ishida, Calculation of the effect of alloying elements on the Ms temperature in steels, J. Alloys Compd. 220 (1995) 126–131.
[22] J.D. Yoo, K.T. Park, Microband-induced plasticity in a high Mn–Al–C light steel, Mater. Sci. Eng. A 496 (2008) 417–424.
[23] E. Welsch, D. Ponge, S.H. Haghighat, S. Sandlöbes, P. Choi, M. Herbig, S. Zaefferer, D. Raabe, Strain hardening by dynamic slip band refinement in a high-Mn lightweight steel, Acta Mater. 116 (2016) 188–199.
[24] M.J. Yao, E. Welsch, D. Ponge, S.M.H. Haghightat, S. Sandlöbes, P. Choi, M. Herbig, I. Bleskov, T. Hickel, M. Lipinska-Chwalek, P. Shanthray, C. Scheu, S. Zaefferer, B. Gault, D. Raabe, Strengthening and strain hardening mechanisms in a precipitation-hardened high-Mn lightweight steel, Acta Mater. 140 (2017) 258–273.
[25] H. Wu, G.H. Fan, An overview of tailoring strain delocalization for strength-ductility synergy, Prog. Mater. Sci. 113 (2020), 100675.
[26] Z. Nishiyama, X-ray investigation of the mechanism of the transformation from face centered cubic lattice to body centered cubic, Sci. Rep. Tohoku Univ. 23 (1934) 637.
[27] O. Grassel, L. Kruger, G. Frommeyer, L.W. Meyer, High strength Fe–Mn–(Al, Si) TRIP/TWIP steels development - properties - application, Int. J. Plast. 16 (2000) 1391.
[28] F. Sun, J.Y. Zhang, M. Marteleur, T. Gloriant, P. Vermaut, D. Laille, P. Castany, C. Curfs, P.J. Jacques, F. Prima, Investigation of early stage deformation mechanisms in a metastable β titanium alloy showing combined twinning-induced plasticity and transformation-induced plasticity effects, Acta Mater. 61 (2013) 6406.
[29] Q. Li, D.Y. Liu, F.K. Yan, N.R. Tao, Martensitic transformation within nanotwins enhances fatigue damage resistance of a nanotwinned austenitic stainless steel, Scripta Mater. 207 (2022), 114313.
[30] M.J. Hytch, E. Snoeck, R. Kilaas, Quantitative measurement of displacement and strain fields from HREM micrographs, Ultramicroscopy 74 (1998) 131–146.

Mr. Jianyang Zhang is a doctoral candidate in the Department of Materials Science and Engineering at the City University of Hong Kong. He obtained his master's degree in 2020 from Tianjin University, China. His current research focuses on the design of high-performance high-entropy alloys with good combination of strength, ductility, and corrosion resistance.

Prof. C.T. Liu is a member of National Academy of Engineering (NAE), USA, and a foreign member of Chinese Academy of Engineering. He is currently a University Distinguished Professor of City University of Hong Kong. He is a world leader in the field of structural metallic materials, focusing on the physical metallurgy and mechanical behaviors of metals and alloys including high-entropy alloys, intermetallic compounds, bulk amorphous alloys and nanostructure materials,

Prof. Yilu Zhao is Full Professor and Doctoral Supervisor in the School of Materials Science and Engineering at the Harbin Institute of Technology (Shenzhen). She received his Ph.D. degree in mechanical engineering from the City University of Hong Kong in 2018. Prof. Zhao's research is working on the advanced microstructural analyses and metallurgical design of high-entropy alloys and intermetallic materials.

Prof. Tao Yang an Assistant Professor of Materials Science and Engineering at the City University of Hong Kong. He was named the National Natural Science Foundation (NSFC) Excellent Young Scientist (Hong Kong and Macau) in 2022. His current research is mainly focused on the innovative design and fabrication of advanced structural materials, including high-entropy alloys, intermetallic materials, and additive manufacturing.